Spatiotemporal evolution of excess pore pressures in a silty seabed under progressive waves during residual liquefaction

Chang-Fei Li [a,b], Yifa Wang [c], Fu-Ping Gao [a,b,*], Li-Jing Yang [a,b]

[a] *Institute of Mechanics, Chinese Academy of Sciences, Beijing 100190, China*
[b] *School of Engineering Science, University of Chinese Academy of Sciences, Beijing 100049, China*
[c] *Department of Infrastructure Engineering, Faculty of Engineering and Information Technology, The University of Melbourne, Melbourne, VIC 3010, Australia*

A R T I C L E   I N F O

A B S T R A C T

Both transient and residual pore pressure responses are induced as ocean waves propagate over a silty seabed. In this study, the spatiotemporal evolution of excess pore pressure in a silty seabed under progressive waves was physically modelled in a large wave flume. Three typical stages were identified in the process of residual liquefaction via flume observations, including quasi-elastic, intensive build-up of residual pore pressure, and continuous liquefaction stages. During the initial quasi-elastic stage before the liquefaction of the silt bed, the transient pore pressure can be well predicted by the analytical solution based on poro-elastic theory. After that, the residual pore pressure builds up intensively to its maximum value, even in the case that the transient pore pressure is nearly negligible at deep soil layer. Once the residual liquefaction occurs, the poro-elastic theory becomes invalid for describing the pore pressure response. The residual liquefaction is not simultaneously induced within the entire bed, but gradually progresses downward from the shallow layer of the silt bed to deeper. The pore pressure amplitude is significantly amplified after the silt liquefies, while no amplitude-amplification was observed within the un-liquefied silt. An amplification ratio (ζ) is proposed to characterize the amplification effect and distinguish the onset of residual liquefaction. The value of ζ during the continuous liquefaction stage is found to be one order of magnitude larger than that in the quasi-elastic stage. Comparisons with the existing centrifuge tests further indicate that the critical cyclic stress ratio for the silt bed is much smaller than that for the sand bed, implying the silt bed is more prone to residual liquefaction.

1. Introduction

Excess pore pressure in the seabed under wave loading may lead to a decrease in effective stress and even seabed liquefaction. In the past few decades, considerable literature has reported the failures of offshore structures caused by seabed liquefaction, such as the instability of breakwaters (de Groot et al., 2006; Jeng, 2018), the sinking or floatation of submarine pipelines (Sumer et al., 1999; Sumer, 2014; Qi et al., 2020), and the instability of offshore platforms (Bea et al., 1983; Li et al., 2011; Gao et al., 2015). Therefore, an accurate evaluation of wave-induced excess pore pressure plays an essential role in the design of marine structures.

The pore pressure responses of a porous seabed under progressive waves, including the transient and residual mechanisms, have been observed in laboratory experiments and field measurements (Zen and Yamazaki, 1990; Sassa and Sekiguchi, 1999; Mory et al., 2007; Li et al.,

2021). Traditionally, these two pore pressure mechanisms were considered individually in the majority of previous studies (e.g. Jeng et al. 2007). The transient pore pressure, which fluctuates with the wave loading, can be described by theoretical models based on poro-elastic theory (Putnam, 1949; Reid and Kajirua, 1957; Moshagen and Tørum, 1975; Yamamoto et al., 1978; Madsen, 1978; Hsu and Jeng, 1994). The corresponding instantaneous liquefaction is essentially induced by the upward seepage force within the upper layer of the seabed under the wave trough. Advances regarding the criteria for instantaneous liquefaction have been made, amongst others, Bear (1972), Zen and Yamazaki (1990) and Qi and Gao (2018). It was recognized that the vertical gradient of excess pore pressure should be identical to the buoyant unit weight of the soil within the instantaneously-liquefied soil layer (Qi and Gao, 2018).

In contrast to instantaneous liquefaction, residual liquefaction of the seabed can be initiated when the effective stress of soil reduces to zero due to the residual pore pressure buildup (Seed and Rahman, 1978;

Notation

c	cohesion of the soil
C_i $(i = 1\text{-}6)$	coefficients in Eqs. (4) and (9)
d	Water depth
d_{10}	effective grain size
d_{50}	mean grain size
D_r	relative density of sands
e	void ratio under the *in-situ* condition
E	energy density in the Fourier spectrum
e_{max}	maximum void ratio
e_{min}	minimum void ratio
f_1	frequency corresponding to the primary peak
f_2	frequency corresponding to the secondary peak
g	gravitational acceleration
G	shear modulus of the soil
G_s	specific weight of the soil
H	wave height
i	imaginary number
I_p	plasticity index
k_s	coefficient of permeability
K'	apparent bulk modulus of the pore-fluid
L	wave length
n	soil porosity
N	number of wave cycles
N_l	number of wave cycles to cause liquefaction
p	wave-induced pore pressure within the soil
$\bar{p}$	residual pore pressure
$\bar{p}_{max}$	maximum residual pore pressure
$\widetilde{p}$	transient pore pressure
p_0	amplitude of wave-induced pressure at the seabed surface
P_b	wave-induced pressure at the seabed surface
s	specific gravity of grains
S_r	degree of saturation
T	wave period
t	time
w	water content of the soil
z	soil depth calculated from the mudline
z_L	limiting liquefaction depth
η	wave surface elevation
α	coefficient in Eq. (5)
δ	coefficient in Eq. (6)
φ	angle of friction
γ'	buoyant unit weight of soil
γ_w	unit weight of water
σ_0'	initial overburden effective stress
λ	wave number
ν	Poisson's ratio
ω	angular frequency of the wave
$|\widetilde{p}|$	amplitude of the transient pore pressure
$|\widetilde{p}|_a$	pore pressure amplitude predicted by Eq. (4)
ζ	amplification ratio
χ	cyclic stress ratio
χ_0	cyclic stress ratio at the seabed surface
χ_{cr}	critical cyclic stress ratio
$\chi_{cr\text{-}sand}$	critical cyclic stress ratio for the sand bed
$\chi_{cr\text{-}silt}$	critical cyclic stress ratio for the silt bed
$|\tau|$	amplitude of wave-induced shear stress

Sumer, 2014). The pore pressure build-up and associated residual liquefaction of the seabed under ocean waves have been extensively investigated through physical modelling (e.g., Foda and Tzang 1994, Sassa and Sekiguchi 1999, Miyamoto et al. 2004, Sumer et al. 2006), theoretical analyses (e.g., Rahman and Jaber 1986, Jeng et al. 2007, Jeng and Seymour 2007), and numerical simulations (e.g., Seed and Rahman 1978, Cheng et al. 2001, Li et al. 2011, Liu et al. 2019, Duan and Wang 2020, Ülker 2021). Sumer et al. (2006) reproduced the complete sequence of silt behaviour beneath progressive waves in a wave flume, though the length of their silt bed (0.9 m) is relatively short compared to the wavelength (2.9 m). In their flume tests, the evolution of the residual pore pressure was highlighted while the transient pore pressure was not discussed. The rapid and substantial increase of the residual pore pressure in the silt bed was also observed in wave flume tests conducted by Foda and Tzang (1994). A significant amplification of the transient pore pressure was monitored during their tests and the soil liquefaction was attributed to the internal resonance event that occurred inside the silt bed. Soil behavior is known to depend on stress level. In a flume test under 1g condition (g is the gravitational acceleration), the soil box is usually shallow and the corresponding stress level is low. Using the centrifuge modelling technique, the wave-induced liquefaction of a fine-grained sand bed under a steady-state centrifugal acceleration of 50g considering viscous scaling law was investigated by Sassa and Sekiguchi (1999). The progressive nature of the soil liquefaction (i. e., the downward advancement of the liquefaction front) was reported, which was accompanied by the amplification of the transient pore pressure. Sumer (2014) found that the build-up of pore pressure in the centrifuge tests is in good agreement with that measured in the 1g flume experiments for shallow soil depths, suggesting the viability of flume tests in physical modelling of wave-induced residual liquefaction. But among most flume and centrifuge tests on wave-induced residual liquefaction, the transient and residual pore pressure mechanisms were

investigated separately. The amplification of the transient pore pressure was measured or noticed previously, but not thoroughly explored.

As for the numerical modellings, Li et al. (2011) proposed a 3D Finite Element Method (FEM) to simulate the wave-induced transient and residual pore pressure around a pile foundation. The effects of wave nonlinearity, soil permeability and pile diameter on the soil response were examined. Liu et al. (2019) developed a mathematical model for accumulation of the wave-induced pore pressure, considering the coupling effect between the development of pore water pressures and evolution of seabed stresses. Such coupling effect could accelerate the pore pressure accumulation. Based on a novel 3D numerical model, Duan and Wang (2020) investigated the wave and current-induced residual seabed response near a single pile. Their numerical results indicated that the wave/current characteristics, soil properties, and pile diameter can significantly affect the residual pore pressures along the vicinity of the pile. Ülker (2021) ever carried out a combined theoretical-numerical study on dynamic response of sandy seabed focusing on nonlinear soil constitutive behavior. The constitutive formulation showed good capability in evaluating the free-field wave-induced dynamic response of sandy seabed and residual liquefaction. However, in much of the previous analytical and numerical modelling of the residual pore pressure, the accompanying transient pore pressure was either assumed to be unchanged or not involved (i.e., the transient and residual pore pressures were not fully coupled). Furthermore, the amplitude amplification of the periodic transient pore pressure during the residual liquefaction process has not been well characterized.

This paper aims to describe the spatiotemporal evolution of wave-induced excess pore pressure in a silty seabed under progressive waves. Wave flume experiments were conducted to investigate the transient and residual pore pressure responses, with typical stages of the pore pressure development identified. The correlation between the spatiotemporal evolution of transient and residual pore pressures is
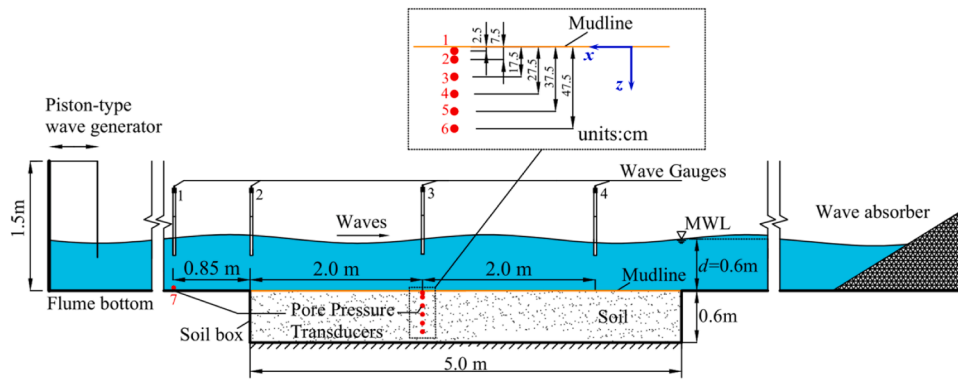
Fig. 1. Schematic diagram of the flume test for wave-seabed interaction.

Table 1
Main physical properties of the test silt.

Soil properties	Symbols (units)	Values
Mean grain size	d_{50} (mm)	0.047
Effective grain size	d_{10} (mm)	0.009
Specific gravity of grains	G_s	2.65
Maximum void ratio	e_{max}	1.14
Minimum void ratio	e_{min}	0.23
Void ratio	e	0.54
Relative density	D_r	0.66
Coefficient of permeability	k_s (m/s)	2.60×10^{-6}
Submerged specific weight of soil	γ' (kN/m^3)	10.71
Plasticity index	I_p	9.0
Cohesion	c (kPa)	6.35
Angle of internal friction	ϕ (°)	27.4

examined. The main characteristics of the silt liquefaction are discussed, with special attention paid to the amplification of the transient pore pressure. This study is expected to provide new insight into the triggering process for wave-induced silt liquefaction.

2. Experimental methodology

2.1. Flume set-up

A wave flume was employed to physically model the excess pore pressure evolution in a silt bed under progressive waves. As illustrated in Fig. 1, the wave flume is 52.0 m in length, 1.0 m in width and 1.5 m in depth. A soil box of 5.0 m (length) × 0.6 m (depth) × 1.0 m (width) is located in the middle of the flume. A piston-type wave maker installed at the inlet of the flume was used to generate progressive waves, while a beach-type wave absorber located at the end of the flume was employed

for an efficient wave absorption with a reflection coefficient less than 5.0%.

As shown in Fig. 1, seven miniature pore pressure transducers (PPTs) were utilized to measure the pore pressures at various depths in the soil (PPT 1 ~ 6) as well as the pressure fluctuation at the flume bottom upstream from the soil box (PPT 7). The probe of the miniature PPT is 5 mm in diameter and 17 mm in length, with a measurement range of 0-20 kPa and an accuracy of 0.2%. To simultaneously monitor the free water surface elevation, four wave gauges (WGs) with the measuring accuracy of 1 mm were located upstream from (WG 1) and above (WG 2 ~ 4) the soil box. The signals of WGs and PPTs were synchronously sampled via a data acquisition system with a sampling frequency of 25 Hz.

2.2. Silt bed preparation

A tube-shaped curtain for linking the trolley bottom and the water surface above soil box was utilized, through which the silt particles can be dropping into the water so that the diffusion of extremely fine particles into the air can be efficiently avoided. The silt-bed surface was then levelled off smoothly with a scraper.

The main physical properties of the silt are summarized in Table 1. Fig. 2 (a) and (b) show the typical morphology of silt grains photographed by scanning electron microscope (SEM) and the particle size distribution curve, respectively. The minimum and the maximum grain sizes of the test silt are approximately 0.2 μm and 0.2 mm, respectively (Fig. 2(b)). The specific gravity of the soil (G_s) was measured by the conventional pycnometer method. The soil samples collected from the silt-bed after deposition in the flume were dried in an oven to obtain the water content (w); The void ratio (e) for a saturated soil can then be obtained as $e = wG_s$ (see Craig 2004). The relative density (D_r) is defined as $D_r = (e_{max} - e)/(e_{max} - e_{min})$, in which e_{max} and e_{min} are the maximum
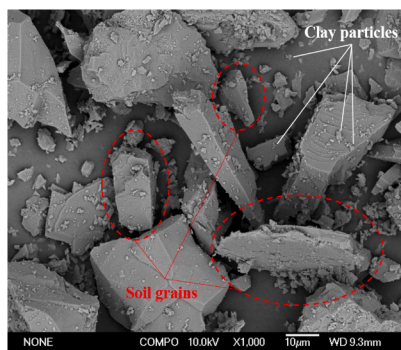
(a)
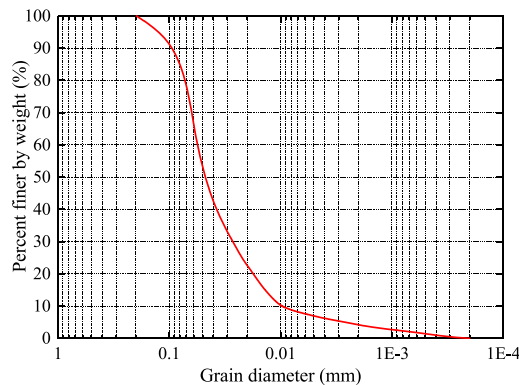
(b)

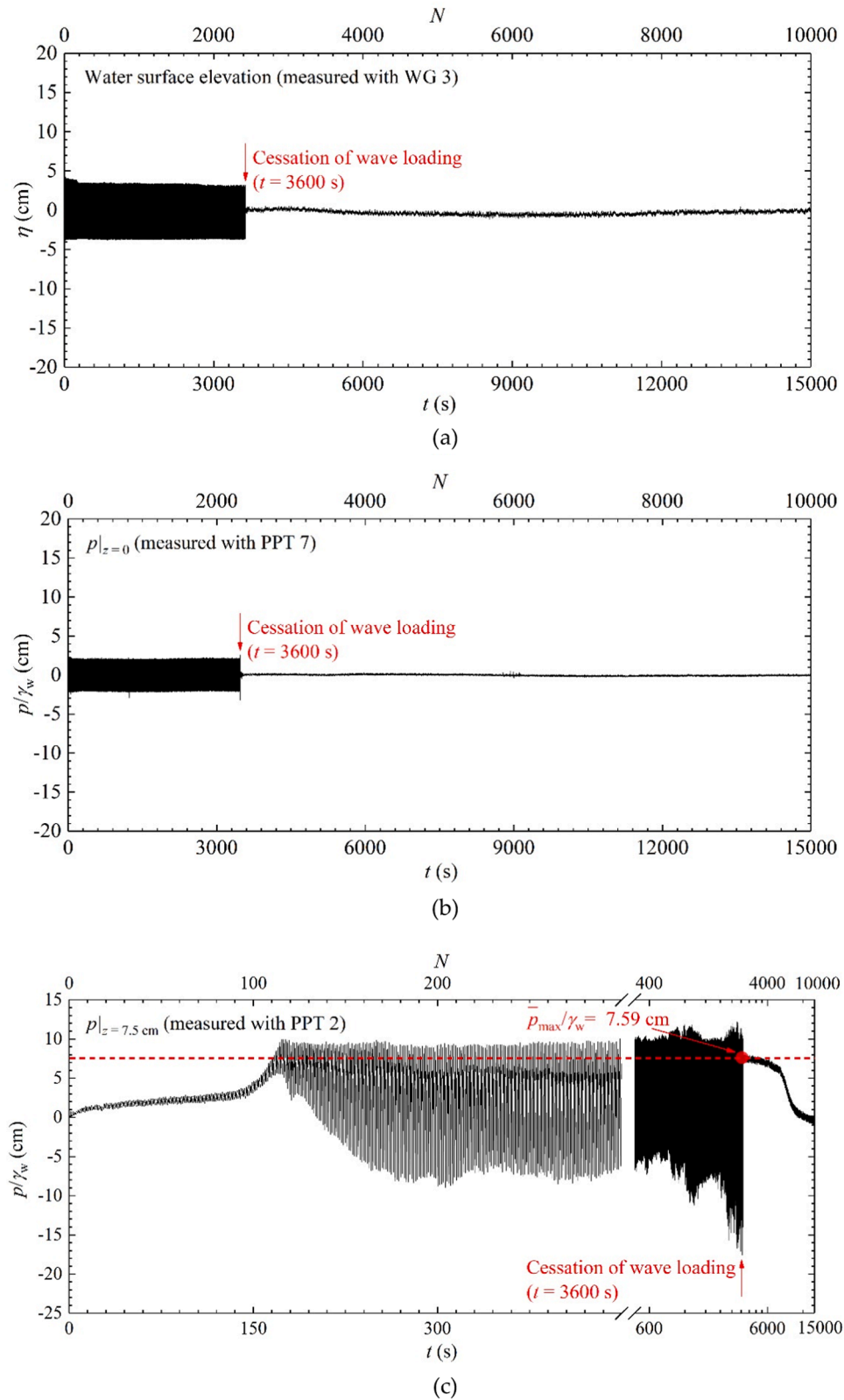**Fig. 2.** Soil grains of the test silt: (a) typical SEM image; (b) particle size distribution.

Fig. 3. Total time series of the water surface elevation (η) and the excess pore pressure (p/γ_w) at two soil depths: (a) η; (b) $z = 0$ (mudline); (c) $z = 7.5$ cm.
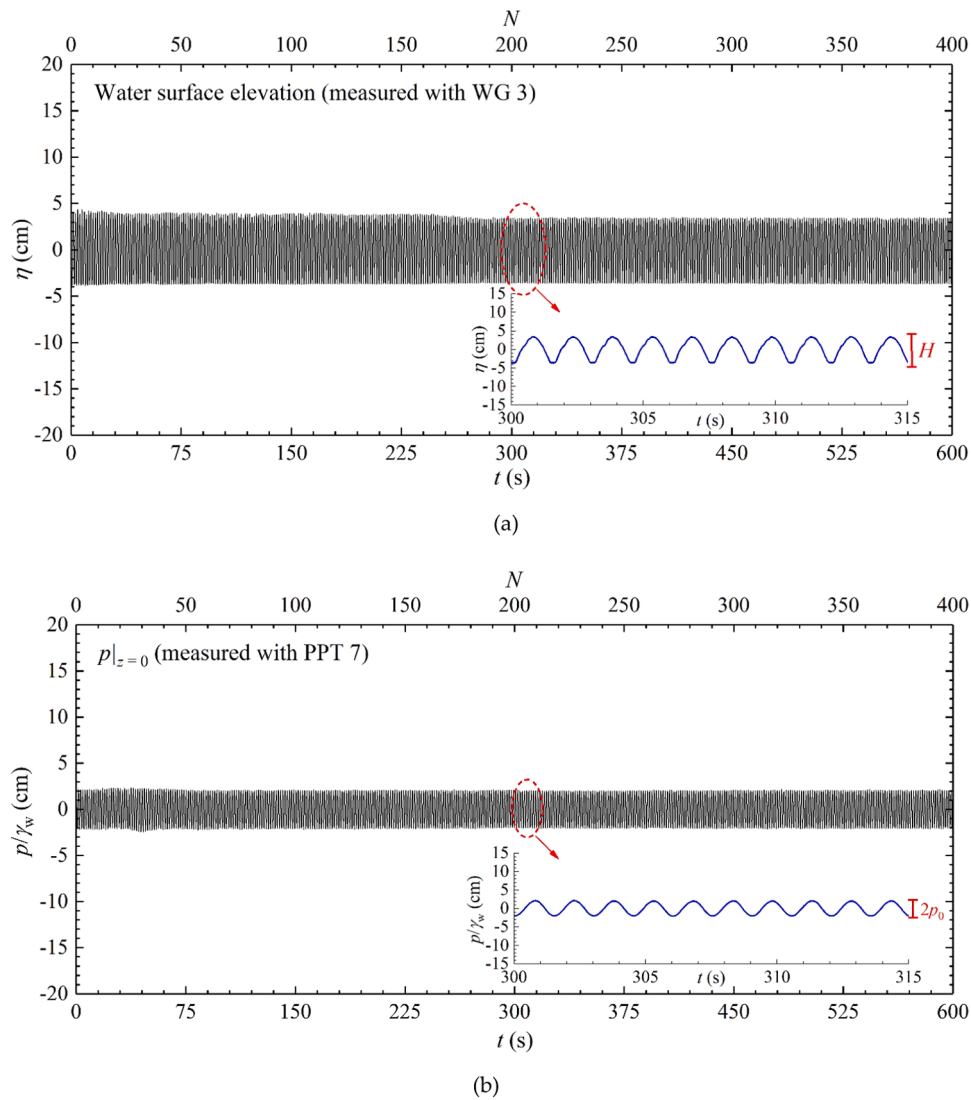
Fig. 4. Time series of the water surface elevation (η) and the excess pore pressure (p/γ_w) at various soil depths: (a) η; (b) $z = 0$; (c) $z = 2.5$ cm; (d) $z = 7.5$ cm; (e) $z = 17.5$ cm; (f) $z = 27.5$ cm; (g) $z = 37.5$ cm; (h) $z = 47.5$ cm.

and the minimum void ratio, respectively. The coefficient of permeability (k_s) was estimated with the empirical equation proposed by Chapius (2004):

$$k_s(\text{cm}/\text{s}) \approx 2.46 \left(\frac{e^3}{1+e} d_{10}^2 \right)^{0.78} \tag{1}$$

where the effective grain size d_{10} is in mm. Note that Eq. (1) is a combination of the Hazen equation and the Kozeny-Carman equation, which can provide a better evaluation of the soil permeability (Chapius, 2004). The measured plasticity index $I_p \approx 9.0$. As I_p increases from 2 to 9, the shear behavior of the silt transforms from sand-like to clay-like material (Boulanger and Idriss, 2006). The cohesion (c) and the angle of internal friction (ϕ) of the silt were determined through triaxial tests. It should be noted that all the values in Table 1 correspond to the pre-test condition, i.e., before the silt bed was subjected to the subsequent series of wave loading.

2.3. Testing procedure

The flume testing procedure involved the following steps:

(1) All PPTs were installed at various soil depths onto a support rack in the soil box (Fig. 1).
(2) The silt bed was carefully prepared by raining the dry silt particles through clean water in the soil box. The soil surface was then levelled with a scraper.
(3) The flume was slowly filled with water to a given depth ($d = 0.6$ m) and kept constant throughout the test.
(4) The piston-type wave maker was activated to generate progressive regular waves, with signals of WGs and PPTs synchronously being logged by the data acquisition system. The wave height (H) and the wave period (T) of regular waves were adopted as $H = 8.0$ cm and $T = 1.5$ s, respectively. Note that the calculated wavelength $L \approx 3.0$ m (< 5.0 m, i.e., the length of the soil box, see Fig. 1), therefore the silt box is sufficiently large to avoid boundary effects. Similarly, in the flume tests for standing waves (Kirca et al., 2013), the length of soil box was equal to one half of the wavelength ($L/2$), so that the soil box was fully exposed to the standing wave.
(5) The wave maker was switched off after the loading duration of 3600 s (one hour), while the data acquisition system was kept logging until the accumulated pore pressure was fully dissipated.
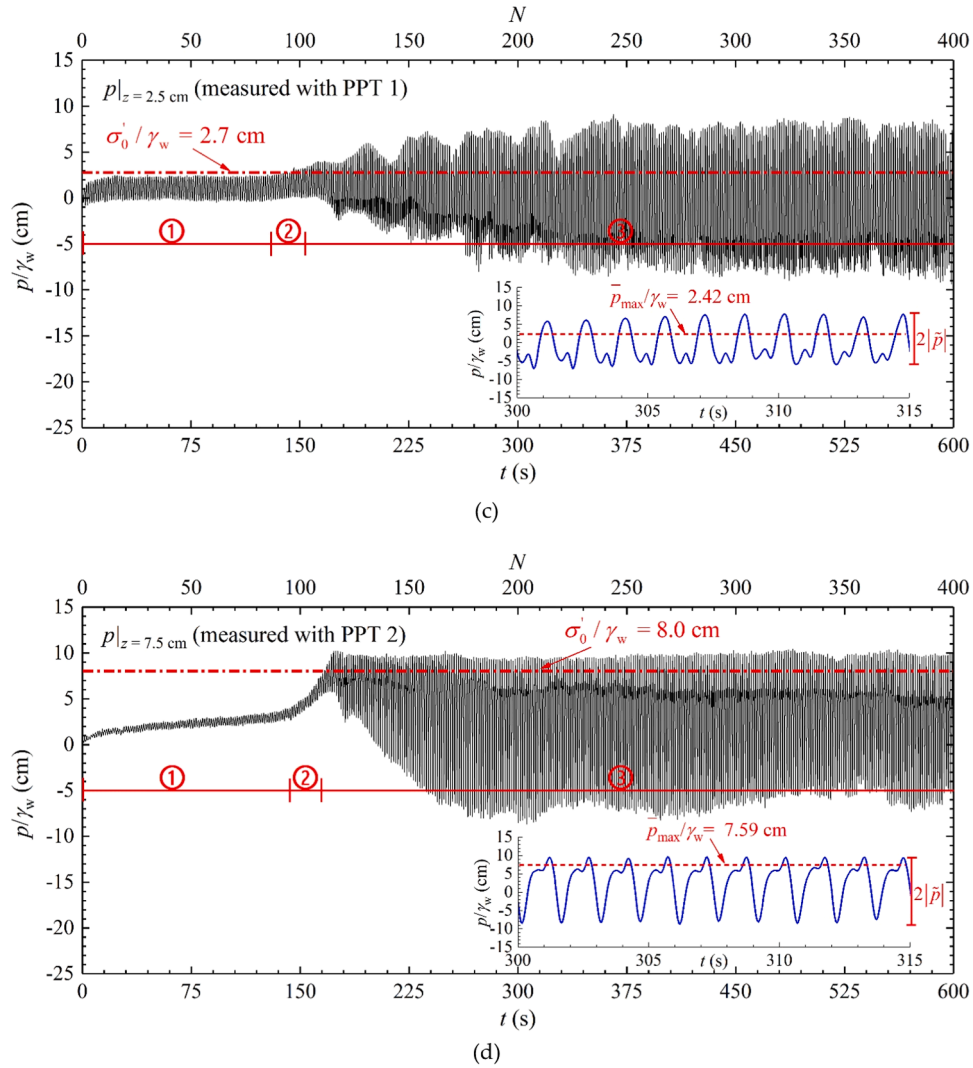
(c)

(d)

Fig. 4. (continued).

3. Results and discussion

3.1. Typical stages during the process of residual liquefaction

In the present flume observations, wave-induced transient ($\widetilde{p}$) and residual ($\overline{p}$) pore pressure responses during the process of silt liquefaction were primarily focused on. For wave-seabed interactions, the wave-induced excess pore pressure in a porous seabed can be generally expressed as:

$$p(x, z, t) = \overline{p}(z, t) + \widetilde{p}(x, z, t) \tag{2}$$

where $\overline{p}$ is the residual pore pressure, and $\widetilde{p}$ is the transient pore pressure.

Fig. 3 shows the time series of the water surface elevation (η) and the corresponding excess pore pressure (p) at two soil depths, i.e., $z = 0$ (mudline), and 7.5 cm, respectively. The number of wave cycles N ($= t/T$) is provided for reference, while the expression p/γ_w is used to keep the same unit as η for comparison, where γ_w ($= 9.8 \times 10^3$ N/m³) is the unit weight of water. As shown in Fig. 3(b), the wave pressure fluctuation at the flume bottom was stable during the action of waves. After the cessation of wave loading (3600 s), the excess pore pressure within the silt bed (z = 7.5 cm) began to dissipate from the maximum residual pore pressure ($\overline{p}_{max}$) to zero (see Fig. 3(c)). To facilitate clear observation of the pore pressures evolution before the waves ceased, the logarithm coordinate was employed for $t > 450$ s in Fig. 3(c). It took more than 3.0

h (from $t = 3600$ s to approximately 15000 s) for the excess pore pressure to be completely dissipated. Note that no obvious dissipation of the pore pressure buildup was observed during the wave loading duration (0 $< t <$ 3600 s), hence the maximum residual pore pressure ($\overline{p}_{max}$) at a certain soil depth can be identified from the data record at the moment when the waves ceased (marked as a red dot in Fig. 3(c)). It should be borne in mind that the wave loadings may retard the dissipation of excess pore pressure but cannot withhold it forever. That is, the silt mudline is not fully impermeable. Eventually, the pore pressure would be dissipated if the duration of wave loading is long enough (see Sumer 2014).

Fig. 4 shows the variations of η measured with WG 3 and the corresponding data of p ($= \overline{p} + \widetilde{p}$, see Eq. (2)) at various soil depths ($z = 0$, 2.5, 7.5, 17.5, 27.5, 37.5, and 47.5 cm) with time (t) or the number of wave cycles (N) during the liquefaction triggering process (e.g., $0 < t <$ 600 s, or $0 < N < 400$). The zoomed-in sections of η and p for 300 s $< t <$ 315 s (i.e., $200 < N < 210$) are also given in Fig. 4. It is indicated that both the measured values of η and the wave pressure on the silt bed (P_b) presented regular and sinusoidal variations (see Fig. 4 (a), (b)). Given the wave parameters ($H = 0.08$ m, $L = 3.0$ m, $d = 0.6$ m), the amplitude of P_b can be calculated with $p_0 = \gamma_w H / 2\cosh(\lambda d)$, where λ ($= 2\pi/L$) is the wave number.

When residual liquefaction occurs, the residual pore pressure ($\overline{p}$) can be assumed to be equal to the initial overburden pressure σ_0' (also termed
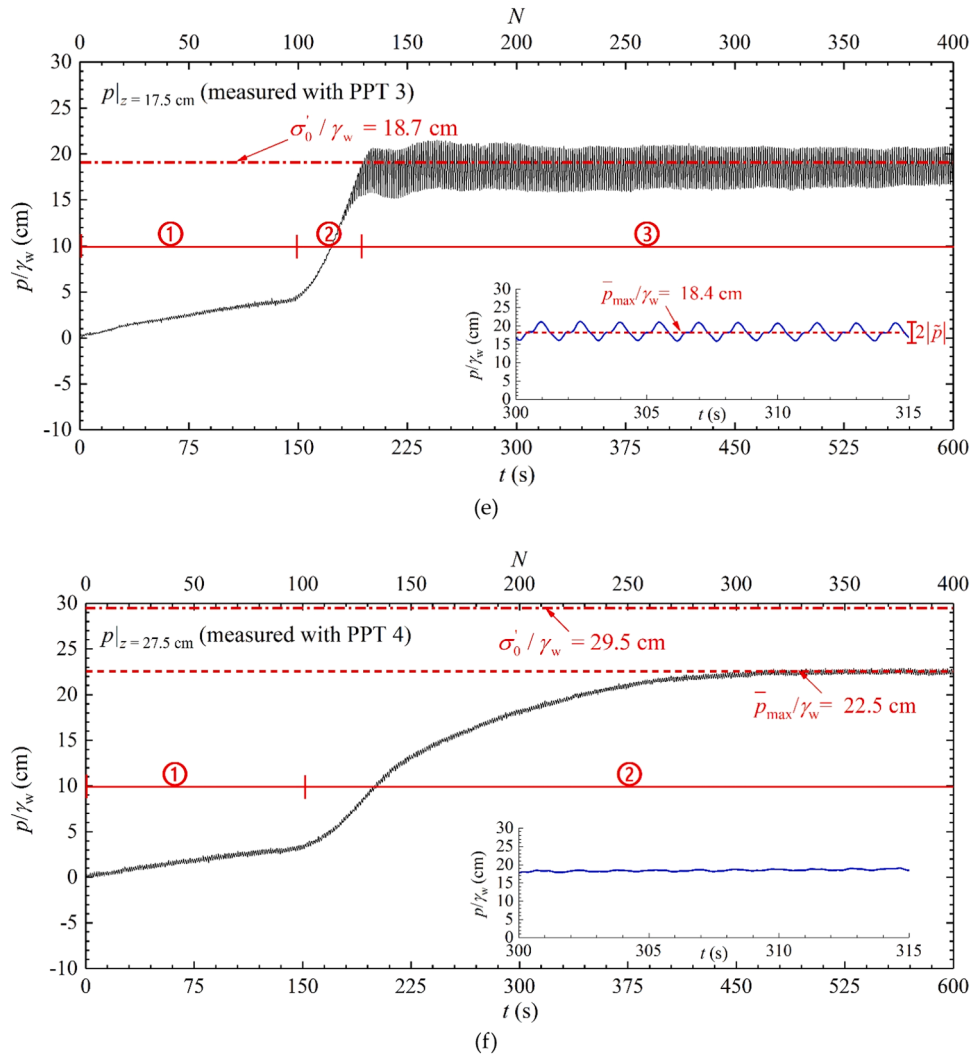
Fig. 4. (*continued*).

the initial vertical effective stress), i.e.,

$$\bar{p} = \sigma_0' \tag{3}$$

where $\sigma_0' = \gamma' z$. Eq. (3) has been adopted by several studies in the past (e. g., Sassa and Sekiguchi 1999, Teh et al. 2003, Miyamoto et al. 2004). As an alternative criteron, $\bar{p}$ has also been set equal to the initial mean normal effective stress (e.g., Jeng et al. 2007, Kirca et al. 2013, Sumer 2014).

The calculated values of σ_0'/γ_w are marked in Fig. 4(c)–(h), along with the maximum residual pore pressure ($\bar{p}_{max}$) and the transient pore pressure amplitude ($|\tilde{p}|$) for 300 s < t < 315 s. It can be seen that the residual pore pressure ($\bar{p}$) accumulates close to the initial overburden pressure (σ_0') for $z \leq 17.5$ cm, while the level of residual pore pressure ($\bar{p}$) is much lower than σ_0' in the deeper soil depths ($z \geq 27.5$ cm). Therefore, the liquefaction criterion allows the limiting liquefaction depth to be identified in the range of 0.175 m < z_L < 0.275 m in Fig. 4. In addition, the number of wave cycles to cause liquefaction (N_l) corresponding to soil depths at z = 2.5 cm, 7.5 cm and 17.5 cm are determined as N_l = 102, 110 and 127, respectively.

Based on the experimental measurements shown in Fig. 4(c)–(h), three typical stages during the triggering process of residual liquefaction can be identified as follows:

Stage-①: Quasi-elastic response: At the beginning of wave loading (e. g., N < 95, see Fig. 4(d)), the pore pressure accumulation was relatively low with minimal plastic soil deformation. The response of the bed to waves can be regarded as quasi-elastic, which is similar to the response of a sand bed (see Yamamoto et al. 1978). The transient pore pressure amplitude attenuated rapidly in the silt bed with increasing soil depth. Such amplitude attenuation will be further discussed in Section 3.2. Moreover, the duration of Stage-① tends to increase with increasing soil depth. Similar soil behavior with Stage-① has also been reported in Sassa et al. (2001) and Sumer et al. (2012). Such soil response was also termed as "no-liquefaction-to-liquefaction transition" (Sumer, 2014). In this stage, lower shear stress ratio was observed in the deeper soil layer, only leading to a gentle rise of residual pore pressure.

Stage-②: Intensive build-up of residual pore pressure: Under the persistent action of waves, the residual pore pressure built up significantly to its maximum value (e.g., 95 < N < 110, see Fig. 4(d)). In this stage, the ultimate residual pore pressure was much higher compared with that in Stage-①, indicating large plastic deformation experienced by the soil. In this stage, the uppermost layer of the silt bed has already been liquefied, the liquefaction front progressed downwards. The two-layer fluid system (water and liquified silt) significantly alters the shear stress in the sub-liquefied soil below the liquefaction front (Sassa et al., 2001), which eventually triggers the intensive build-up of residual pore pressure. Moreover, Stage-② would last until the waves finally ceased in the un-liquefied layer despite negligible transient pore pressure (e.g., $z \geq 27.5$ cm, see Fig. 4(f)–(h)).

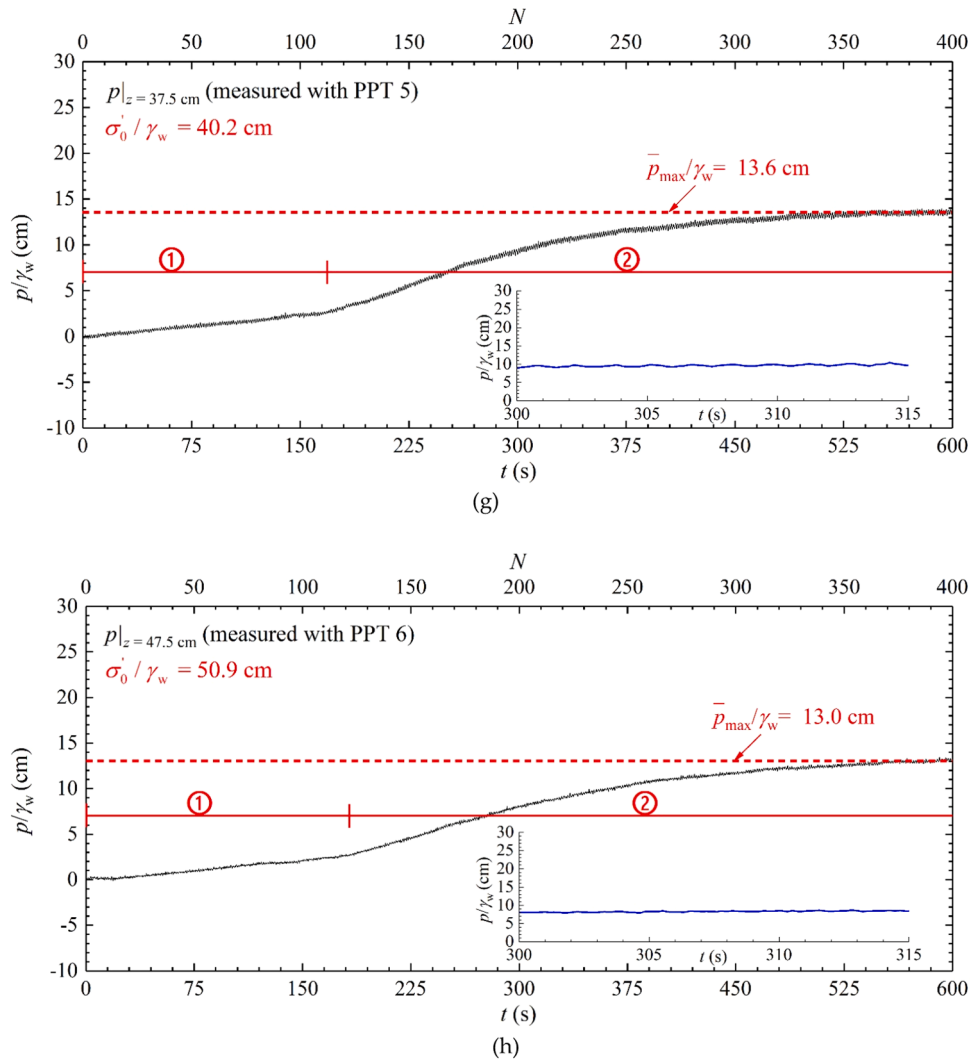*Stage-③: Continuous liquefaction*: Once the residual pore pressure

(g)

(h)

Fig. 4. (*continued*).

reached the initial overburden effective stress at a certain depth, the silt bed was liquefied (e.g., $N > 110$, see Fig. 4(d)). In this stage, the transient pore pressure at $z \leq 17.5$ cm was amplified and no longer sinusoidal. Meanwhile, the residual pore pressure was maintained at its maximum value (see Fig. 4(c)–(e)). However, such amplification phenomenon of Stage-③ was not recognized in the un-liquefied soil ($z \geq$ 27.5 cm, see Fig. 4(f)–(h)). The amplitude-amplification of transient pore pressures will be detailed in Section 3.3.

It should be noted that the observed three stages depict a special case for a moderate wave height. Such typical stages the silt may experience depend on not only soil depths (see Fig. 4(c)–(h)), but also wave heights. For instance, in the case of a smaller wave height (no liquefaction would
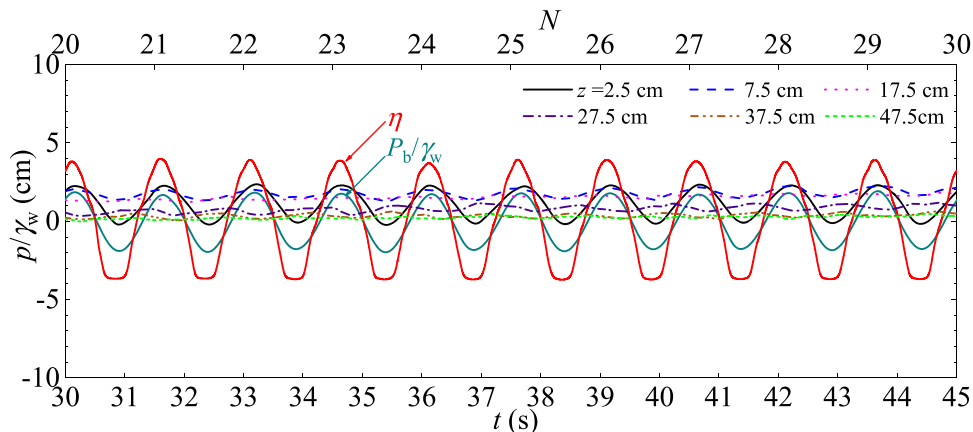

Fig. 5. Time series of the wave-induced pore pressure at various depths for $20 < N < 30$.
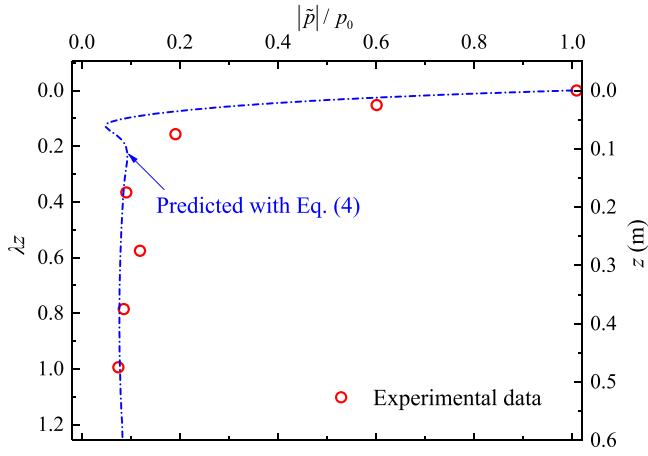
Fig. 6. Comparison of the amplitude attenuation of wave-induced transient pore pressure in the silty bed between experimental data and analytical prediction ($N<30$).

appear), the soil behavior would merely include Stage-①. By contrast, in the case of a larger wave height, the soil would undergo higher shear stress ratio during the initial period of the wave loading, so that Stage-② and Stage-③ could be dominant.

Moreover, the boundary effects from the side walls and the bottom of the soil box in a flume test could be influential in the triggering process of silt liquefaction. In the previous experiments by Sumer et al. (1999), (2006), the silt was placed in a box with a depth of 0.17 m, and a length of 0.9 m, and about the same width (0.5 m) as the flume. In comparison with the present tests, the sizes of their soil box are much smaller than the present ones, and the boundary effects could be non-negligible. In the experiments by Sumer et al. (2006), the gentle rise of residual pore pressure in Stage-① was not identified, and the build-up of residual pore pressure (Stage-②) was much quicker (e.g., $N < 10$) than the present observations; meanwhile, the amplitude-amplification of transient pore pressure was not significant.

3.2. Quasi-elastic response of the silt bed

The variations of transient pore pressure in Stage-① are examined in this section. Fig. 5 shows the typical time series of the wave-induced pore pressure at various soil depths for $20<N<30$. The wave surface elevation (η) and the wave pressure fluctuation on the seabed (P_b) are also included for comparison. Note that P_b was measured in the far-field and thus was transformed to match the phase of η. It can be seen that the amplitude of the transient pore pressure attenuated significantly across the soil depth.

To examine the behavior of the transient pore pressure before soil liquefaction, experimental results are compared with available analytical solutions. The wave-induced transient pore pressure in an isotropic seabed with finite thickness can be expressed as (Hsu and Jeng, 1994):

$$p(z)=\frac{P_b}{1-2\nu}\left\{(1-\alpha-2\nu)\left(C_2 e^{-\lambda z}-C_4 e^{\lambda z}\right)+(1-\nu)\left(\delta^2-\lambda^2\right)\left(C_5 e^{-\delta z}+C_6 e^{\delta z}\right)\right\}$$
(4)

where$P_b = p_0 exp[i(\lambda x + \omega t)]$is the wave pressure fluctuation at the seabed surface, and i is the imaginary number. The expressions of $\alpha$and δ for an isotropic bed are as follows:

$$\alpha=\frac{n(1-2\nu)}{K'\left(\frac{n}{K'}+\frac{1-2\nu}{G}\right)}$$
(5)

$$(\delta)^2=\lambda^2+i\frac{\gamma_w}{k_s}\omega\left(\frac{1-2\nu}{2(1-\nu)G}+\frac{n}{K'}\right)$$
(6)

where K' is the apparent bulk modulus of the pore-fluid, G and ν are the shear modulus and the Poisson's ratio of the soil, respectively; n (= $e/1+e$) is the soil porosity. The details of the parameters C_2, C_4, C_5, C_6 in Eq. (4) can be referenced in Hsu and Jeng (1994).

Fig. 6 compares the amplitude attenuation between the analytical prediction and the experimental data. Note that only the first 30 pore pressure cycles (i.e., $N < 30$) were adopted to identify the averaged amplitude attenuation. The shear modulus (G), the Poisson's ratio (ν) and the degree of saturation (S_r) of the soil adopted in Eq. (4) are: $G = 10.0$ MPa, $\nu = 0.30$ and $S_r = 0.996$, respectively. As shown in Fig. 6, Eq. (4) generally provides a good prediction of the pore pressure amplitudes, demonstrating the validity of poro-elastic theory for describing the pore pressure response in Stage-①. The pore pressure amplitudes for $z > 7.5$ cm rapidly attenuated to $|\tilde{p}|/p_0 < 0.1$(see Fig. 6), indicating the boundary effects were not obvious under the present test condition. In addition, the amplitude attenuation in the silt bed is more significant than that in the sand bed (see Qi et al., 2019; Li and Gao, 2022), which can be mainly attributed to the lower permeability and higher compressibility of the silt.

3.3. Amplitude-amplification of the transient pore pressure

As aforementioned in Section 3.1, the transient pore pressure was amplified after the liquefaction was triggered (i.e., Stage-③). Fig. 7 shows the excess pore pressure response in proximity to the onset of residual liquefaction. A slight but discernible amplification of transient pore pressure can be observed when N approaches N_l in Stage-②, as marked with a dashed circle in Fig. 7. Importantly, the amplification aggravated after liquefaction started. Fig. 8 shows the time series of the excess pore pressure at those liquefied soil depths ($z = 2.5$ cm, 7.5 cm and 17.5 cm) for $200 < N < 210$. The variations of η and P_b are also plotted for comparison. In contrast to the response before liquefaction (Fig. 5), the pore pressure within the liquefied soil becomes non-sinusoidal but still periodic. Meanwhile, the pore pressure amplitude ($|\tilde{p}|$) may exceed the wave pressure amplitude on the seabed (p_0) and no longer attenuates with the soil depth, which is out of the scope of the poro-elastic theory.

While the residual pore pressure was maintained at its maximum value ($\bar{p}_{max}$) in Stage-③, it was not the center axis of the pore pressure oscillation at $z = 2.5$ cm and 7.5 cm (see Figs. 4(c), (d) and (8)). In other words, the residual pore pressure was no longer the period-averaged excess pore pressure, with the mean value being approximately zero. Negative pore pressure was presented in the asymmetric waveform within the upper liquefied silt. Such negative oscillations with excessive drops of the pore pressure were attributed to the suction from the top silt layer associated with the passage of wave troughs (Kirca et al., 2014). In contrast, the pore pressure in the deeper soil (e.g., at $z = 17.5$ cm) was still symmetric and positive about the maximum residual pore pressure $\bar{p}_{max}$(see Figs. 4(e) and (8)).

The periodic but irregular oscillations in Fig. 8 may comprise several harmonic ones. Fourier analysis is conducted to examine the potential superposition of waveforms. Based on the measured pore pressure data in Fig. 8, the Fourier spectra of the pore pressures at various soil depths are given in Fig. 9. E is the energy density of the pore pressure spectrum in cm^2/Hz, as the expression p/γ_w is employed in Fig. 8. As shown in Fig. 9, two distinct peaks of the energy density can be identified in the frequency-domain of the amplified transient pore pressures, i.e., a primary peak and a secondary peak. The frequencies corresponding to the primary and secondary peaks are f_1 and f_2, respectively (see Fig. 9(a)–(c)). The values of f_1 and f_2 are consistent for all the double-peak spectra. Moreover, the value of f_1 is identical to the frequency of the surface waves, i.e., $f_1 = 1/T$, where T (= 1.5 s) is the wave period. Thus, the apparent period of the excess pore pressure is also 1.5 s, as shown in Fig. 8. Moreover, the value of f_2 is exactly twice the value of f_1, i.e., $f_2 = 2 f_1$. As expected, the higher harmonic in the pore pressure spectra (Fig. 9
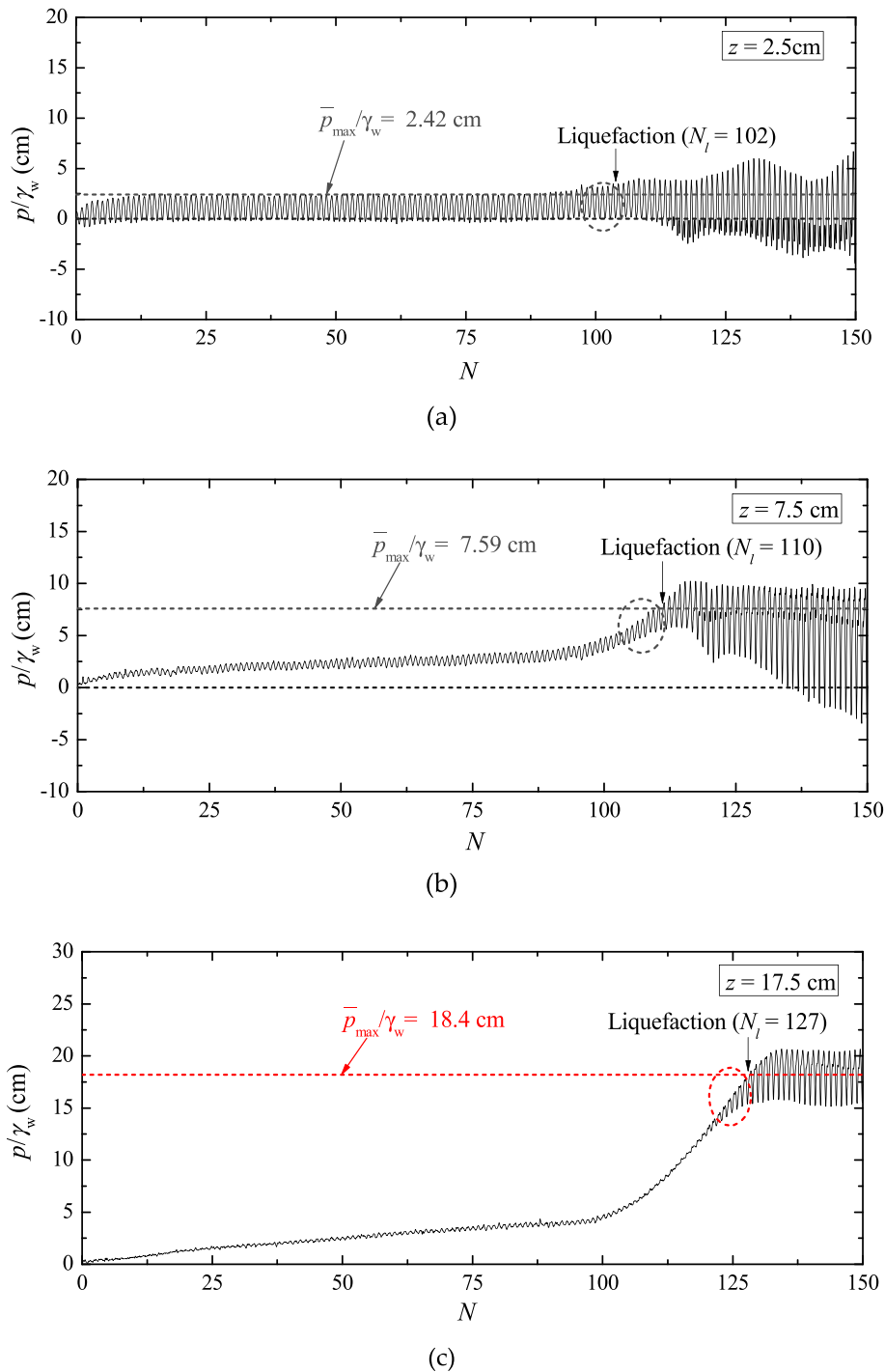
Fig. 7. The excess pore pressure response in proximity to the onset of liquefaction: (a) $z = 2.5$ cm; (b) $z = 7.5$ cm; (c) $z = 17.5$ cm.

(b)–(d)) is inherent from the non-linearity of the wave loading (Fig. 9 (a)). It is indicated that the high-frequency components of the wave loading were significantly amplified within the liquefied layer (Fig. 9(b) and (c)).

To quantify the pore pressure after soil liquefaction, a dimensionless amplification ratio (ζ) is introduced as:

$$\zeta = \frac{|\widetilde{p}|}{|\widetilde{p}|_a} \qquad (7)$$

where ζ is the amplification ratio, $|\widetilde{p}|$ is the measured amplitude of the transient pore pressure at a certain soil depth, while $|\widetilde{p}|_a$ is the

corresponding amplitude of the transient pore pressure predicted by Eq. (4). That is, ζ characterizes the relative magnitude of the actual pore pressure amplitude to the predicted pore pressure amplitude in the quasi-elastic stage (Stage-①). For $\zeta = 1.0$, the ratio corresponds to the case that the transient pore pressure is not amplified and can be perfectly predicted by the poro-elastic theory. Fig. 10 shows the amplification ratio (ζ) with the number of wave cycles (N) in the liquefied ($z \leq 17.5$ cm) and un-liquefied soil ($z \geq 27.5$ cm). The three typical stages identified in Section 3.1 are also marked in Fig. 10(a). Within the liquefied soil depth (see Fig. 10(a)), the variations of ζ with N are significantly affected by the occurrence of residual liquefaction. During the quasi-elastic stage (Stage-①), it is indicated that $\zeta \approx 1.0$. The values of ζ in
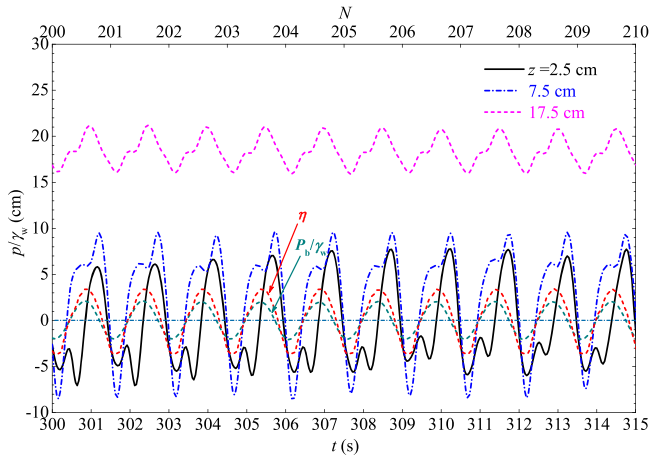
Fig. 8. Time series of the wave-induced pore pressure at various liquefied soil depths ($200<N<210$).

Stage-① and earlier Stage-② are nearly identical. At later Stage-② (i.e., in proximity to the onset of residual liquefaction), the value of ζ would slightly increase with the number of wave cycles, which has also been presented in Fig. 7. Such an increase of ζ in Stage-② is more significant in the deeper layer (e.g. $120 < N < 127$ for $z = 17.5$ cm). Once the soil is liquefied (Stage-③), the value of ζ would increase significantly at earlier Stage-③ (e.g., $110 < N < 200$ for $z = 7.5$ cm), and then becomes relatively stable (e.g., $N > 200$). The ultimate (or maximum) value of ζ is much larger than 1.0, which can be one of the phenomenological criteria for the liquefaction of a silt bed. In addition, the variations of ζ are generally more disordered in the shallow layer of the silt bed (e.g., at $z = 2.5$ cm, 7.5 cm) than those in the lower layer (e.g., at $z = 17.5$ cm). In the un-liquefied soil (see Fig. 10(b)), the value of ζ is much smaller, owing to the marginal oscillation amplitude (see Fig. 4(f)–(h)). Fig. 11 shows the vertical distributions of the average amplification ratio of the transient pore pressures (ζ) for $20 < N < 30$, $120 < N < 130$ and $200 < N < 210$, providing a comprehensive perspective on the pore pressure amplification during residual liquefaction. It is indicated that the value of ζ could become an order of magnitude larger after residual liquefaction. Below the liquefaction front ($z \geq 27.5$ cm), the value of ζ only increases slightly compared with the scenario of Stage-①. Together with the liquefaction criterion (Eq. (3)), the amplification ratio (ζ) could be another indicator to symbolize the residual liquefaction in a silt bed.

Sassa and Sekiguchi (1999) also reported amplification of the transient pore pressure in a sand bed. Such amplification phenomenon was observed below the front of residual liquefaction, i.e., in the un-liquefied sand layer. Nevertheless, in the present tests, it was observed that the pore pressure amplitude was amplified in the upper liquefied silt layer.

3.4. Spatiotemporal progress of residual liquefaction

To illustrate the progressive nature of the residual liquefaction, Fig. 12 shows the vertical distribution of the residual pore pressure ($\bar{p}$) with different numbers of wave cycles that cause liquefaction (N_l). Within the liquefied soil zone, the residual pore pressure was identical to the overburden effective stress. The residual liquefaction was initiated in shallower soil depths and progressed downward to the deeper seabed. Eventually, the maximum liquefaction depth was achieved and the residual pore pressure remained constant at $\bar{p}_{max} = \gamma' z$. Similar to the previous experiments (e.g., Sumer et al. 2006, Kirca 2013), the wave-induced pore pressure in the present silt bed was measured only in the vertical direction, which was aimed to observe the propagation of residual liquefaction front. Numerical simulation by Jeng and Zhao (2014) indicated that, the liquefaction zone related to the initial incident of the progressive wave phases was formed as a two-dimensional pattern
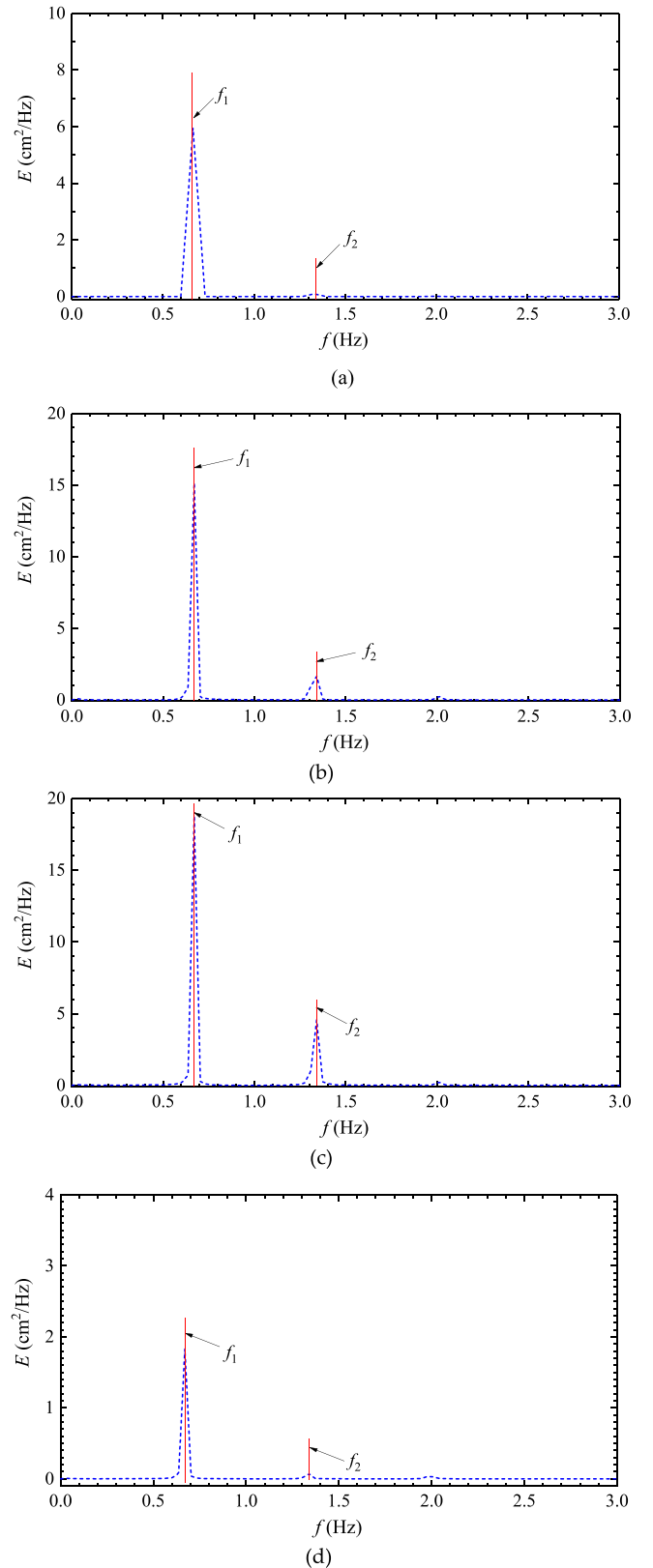

Fig. 9. Fourier spectra of (a) the wave surface elevation, and the transient pore pressures at various soil depths based on the measured data shown in Fig. 8: (b) $z = 2.5$ cm; (c) $z = 7.5$ cm; (d) $z = 17.5$ cm.
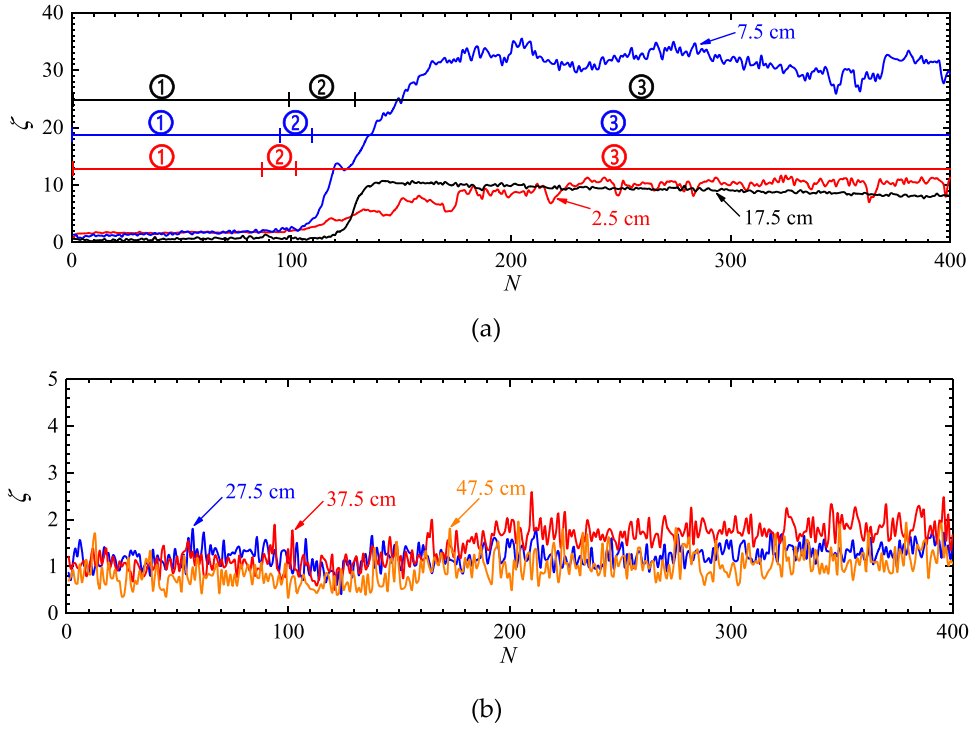
(a)

(b)

Fig. 10. The development of the amplification ratio of transient pore pressures (ζ) with the number of wave cycles (N): (a) in the liquefied soil; (b) in the un-liquefied soil..
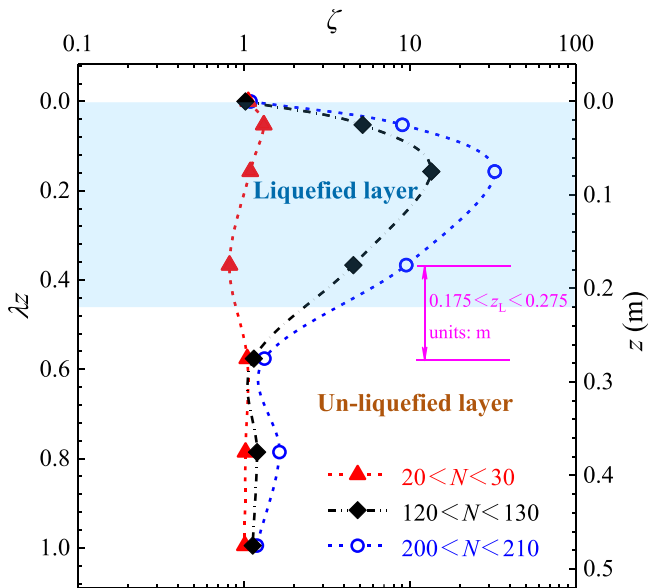

Fig. 11. Vertical distribution of the amplification ratio of transient pore pressures (ζ) for $20 < N < 30$, $120 < N < 130$ and $200 < N < 210$.

Fig. 12. Vertical distribution of residual pore pressure ($\bar{p}$) with various numbers of wave cycles that cause liquefaction (N_l).

during the initial liquefaction period (e.g., $t/T = 90$ in their example), which became one-dimensional pattern after a number of wave cycles.

The severity of progressive wave loading acting on a seabed may be expressed in terms of the cyclic stress ratio χ (Sassa and Sekiguchi, 1999), defined as

$$\chi = \frac{|\tau|}{\sigma_0'} \tag{8}$$

where $|\tau|$ is the amplitude of wave-induced shear stress at that horizon, and $\sigma_0'(= \gamma' z)$ is the initial vertical effective stress there. Based on the
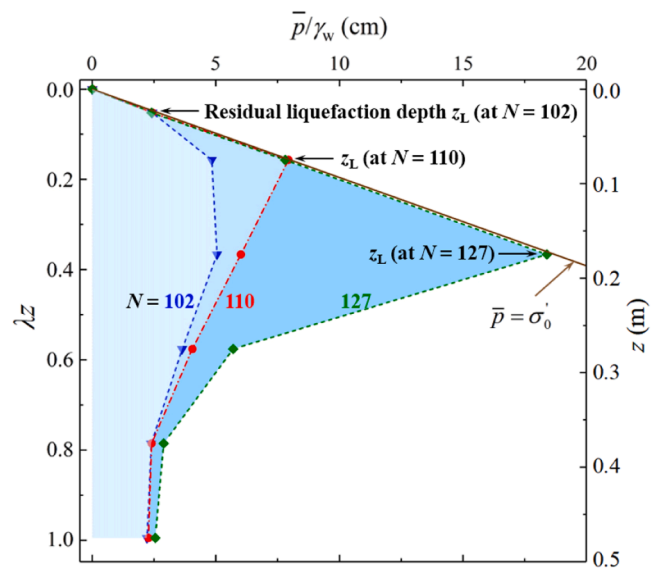
classical poro-elastic theory, it follows that (Hsu and Jeng, 1994)

$$\tau = iP_b\left\{[C_1 - (\lambda z + \alpha)C_2]e^{-\lambda z} - [C_3 + (\alpha - \lambda z)C_4]e^{\lambda z} + \lambda\delta(C_5 e^{-\delta z} - C_6 e^{\delta z})\right\} \tag{9}$$

Fig. 13 gives the vertical distribution of the normalized shear stress amplitude ($|\tau|$) and cyclic stress ratio (χ) along the soil depth. It is indicated that the severity of the progressive waves exerted on a seabed would attenuate along the soil depth. As such, the soil in the shallow layer of the silt bed is more susceptible to liquefaction, resulting in the increased value of N_l with increasing soil depth (z). Especially, the stress ratio χ reaches its maximum value $\chi_0 = 0.04$ at the mudline ($z = 0$).
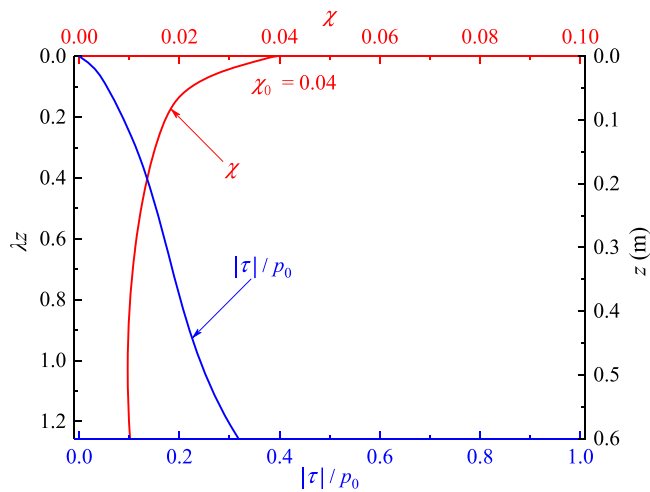
Fig. 13. Vertical distribution of the shear stress amplitude ($|\tau|$) and cyclic stress ratio (χ) in the silt bed.

The critical cyclic stress ratio χ_{cr} can be employed to denote the threshold of χ_0 for the onset of residual liquefaction (Sassa and Sekiguchi, 1999). When $\chi_0 < \chi_{cr}$, there only exists slightly plastic behavior and residual liquefaction hardly occur, and vice versa. In their centrifuge tests, the value of $\chi_{cr-sand}$ proved to be 0.14 for the loose sand. Under the present test condition for a silt bed (Table 1), the flume results suggest

$$\chi_{cr-silt} \leq \chi_0 = 0.04 (< \chi_{cr-sand} = 0.14) \tag{10}$$

Considering the critical stress ratio of the silt bed ($\chi_{cr-silt}$) is significantly smaller than that of the sand bed ($\chi_{cr-sand}$), it is reasonable to infer that the silt bed is more prone to residual liquefaction than the sand bed under a given wave loading. The residual liquefaction of a sand bed can hardly be reproduced in a wave flume, which may be attributed to the relatively large critical stress ratio.

4. Conclusions

This study presents large wave flume test designed to investigate the spatiotemporal evolution of excess pore pressure in a silty seabed under progressive waves. Two mechanisms of the pore pressure response, i.e., the transient and residual pore pressure, are examined to understand the silt liquefaction subjected to ocean wave loading, which is of great importance for the safety of marine structures. The principal conclusions can be drawn as follows.

(1) Three typical stages can be identified in the process of residual liquefaction, including quasi-elastic, intensive build-up and continuous liquefaction stages. During the quasi-elastic stage, an amplitude attenuation phenomenon has been observed for the transient pore pressure, which can be well predicted by the conventional poro-elastic theory. The residual pore pressure accumulates significantly to its maximum value in the intensive build-up stage, while the transient pore pressure amplitude may be negligible.

(2) The transient pore pressure is significantly amplified after the silt liquefies, while no amplification effect can be identified in the unliquefied silt. Double-peak modes were observed in the frequency domain of the amplified transient pore pressure. Once the negative pore pressure is induced in the continuous liquefaction stage, the period-averaged excess pore pressure would no longer be identical to the maximum residual pore pressure.

(3) An amplification ratio (ζ) is proposed to characterize the amplification effect and distinguish the onset of residual liquefaction.

The value of ζ is found to be one order of magnitude larger during residual liquefaction than that in the quasi-elastic stage.

(4) Comparison with the existing centrifuge tests shows that the critical cyclic stress ratio (χ_{cr}) of the silt bed is smaller than that of the sand bed, indicating that the silt bed is more prone to residual liquefaction under progressive wave loading.

CRediT authorship contribution statement

Chang-Fei Li: Writing – original draft, Investigation, Formal analysis, Writing – review & editing. **Yifa Wang:** Validation, Formal analysis, Writing – review & editing. **Fu-Ping Gao:** Conceptualization, Writing – review & editing, Supervision. **Li-Jing Yang:** Investigation, Writing – review & editing.

Declaration of Competing Interest

The authors declare that they have no known competing financial interests or personal relationships that could have appeared to influence the work reported in this paper.

Data availability

No data was used for the research described in the article.

Acknowledgments

References

Bea, R.G., Wright, S.G., Sircar, P., et al., 1983. Wave-induced slides in south pass block 70, Mississippi delta. J. Geotech. Eng. 109 (4), 619–644. ASCE.

Bear, J., 1972. Dynamics of Fluids in Porous Media. Courier Dover Publications, Dove.

Boulanger, R.W., Idriss, I.M., 2006. Liquefaction susceptibility criteria for silts and clays. J. Geotech. Geoenviron. Eng. 132 (11), 1413–1426.

Chapuis, R.P., 2004. Predicting the saturated hydraulic conductivity of sand and gravel using effective diameter and void ratio. Can. Geotech. J. 41 (5), 787–795.

Cheng, L., Sumer, B.M., Fredsøe, J., 2001. Solutions of pore pressure build up due to progressive waves. Int. J. Numer. Anal. Methods Geomechics 25, 885–907.

Craig, R.F., 2004. Craig's Soil Mechanics, 7th ed. E & FN Spon, London & New York.

de Groot, M.B., M, K., Meijers, P., Oumeraci, H., 2006. Liquefaction phenomena underneath marine gravity structures subjected to wave loading. J. Waterw. Port Coast. Ocean Eng. 132, 325–335.

Duan, L., Wang, D., 2020. Novel three-dimensional numerical model for residual seabed response to natural loadings near a single pile. Appl. Ocean Res. 94, 102004.

Foda, M.A., Tzang, S.Y., 1994. Resonant fluidization of silty soil by water waves. J. Geophys. Res. 99 (C10), 20463–20475.

Gao, F.P., Li, J.H., Qi, W.G., Hu, C., 2015. On the instability of offshore foundations: theory and mechanism. Sci. China Phys. Mech. Astron. 58 (12), 124701.

Hsu, J.R.C., Jeng, D.S., 1994. Wave-induced soil response in an unsaturated anisotropic seabed of finite thickness. Int. J. Numer. Anal. Methods Geomech. 18 (11), 785–807.

Jeng, D.S., Seymour, B.R., 2007. Simplified analytical approximation for pore-water pressure buildup in marine sediments. J. Waterw. Port Coast. Ocean Eng. 133 (4), 309–312.

Jeng, D.S., Seymour, B., Gao, F.P., Wu, Y.X., 2007. Ocean waves propagating over a porous seabed: residual and oscillatory mechanisms. Sci. China Ser. E Technol. Sci. 50 (1), 81–89.

Jeng, D.S., 2018. Mechanics of Wave-Seabed-Structure Interactions: Modelling, Processes and Applications. Cambridge University Press, Cambridge.

Jeng, D.S., Zhao, H.Y., 2014. Two-dimensional model for accumulation of pore pressure in marine sediments. J. Waterw. Port Coast. Ocean Eng. 141 (3), 04014042.

Kirca, V.S.O., 2013. Sinking of irregular shape blocks into marine seabed under wave-induced liquefaction. Coast. Eng. 75, 40–51.

Kirca, V.S.O., Sumer, B.M., Fredsøe, J., 2013. Residual liquefaction of seabed under standing waves. J. Waterw. Port Coast. Ocean Eng. 139 (6), 489–501.

Kirca, V.S.O., Sumer, B.M., Fredsøe, J., 2014. Influence of clay content on wave-induced liquefaction. J. Waterw. Port Coast. Ocean Eng. 140 (6), 04014024.

Li, C.F., Gao, F.P., 2022. Characterization of spatio-temporal distributions of wave-induced pore pressure in a non-cohesive seabed: amplitude-attenuation and phase-lag. Ocean Eng. 253, 111315.

Li, C.F., Gao, F.P., Yang, L.J., 2021. Breaking-wave induced transient pore pressure in a sandy seabed: flume modeling and observations. J. Mar. Sci. Eng. 9 (2), 160.

Li, X.J., Gao, F.P., Yang, B., Zang, J., 2011. Wave-induced pore pressure responses and soil liquefaction around pile foundation. Int. J. Offshore Polar Eng. 21 (3), 233–239.

Liu, X.L., Cui, H.N., Jeng, D.S., Zhao, H.Y., 2019. A coupled mathematical model for accumulation of wave-induced pore water pressure and its application. Coast. Eng. 154, 103577.

Madsen, O.S., 1978. Wave-induced pore pressures and effective stresses in a porous bed. Geotechnique 28 (4), 377–393.

Miyamoto, J., Sassa, S., Sekiguchi, H., 2004. Progressive solidification of a liquefied sand layer during continued wave loading. Geotechnique 54 (10), 617–629.

Mory, M., Michallet, H., Bonjean, D., et al., 2007. A field study of instantaneous liquefaction caused by waves around a coastal structure. J. Waterw. Port Coast. Ocean Eng. 133 (1), 28–38.

Moshagen, H., Torum, A., 1975. Wave induced pressures in permeable seabeds. J. Waterw. Harb. Coast. Eng. Div. 101 (4), 49–57. ASCE.

Putnam, J.A., 1949. Loss of wave energy due to percolation in a permeable sea bottom. Trans. Natl. Saf. Congr. Eos Trans. Am. Geophys. Union 30 (3), 349–356.

Qi, W.G., Gao, F.P., 2018. Wave induced instantaneously-liquefied soil depth in a non-cohesive Seabed. Ocean Eng. 153, 412–423.

Qi, W.G., Li, C.F., Jeng, D.S., Gao, F.P., Liang, Z.D., 2019. Combined wave-current induced excess pore-pressure in a sandy seabed: flume observations and comparisons with theoretical models. Coast. Eng. 147, 89–98.

Qi, W.G., Shi, Y.M., Gao, F.P., 2020. Uplift soil resistance to a shallowly-buried pipeline in the sandy seabed under waves: poro-elastoplastic modeling. Appl. Ocean Res. 95, 102024.

Rahman, M.S., Jaber, W.Y., 1986. A simplified drained analysis for wave-induced liquefaction in ocean floor sands. Soils Found. 26 (3), 57–68.

Reid, R.O., Kajiura, K., 1957. On the damping of gravity waves over a permeable sea bed. Trans. Natl. Saf. Congr. Eos Trans. Am. Geophys. Union 30 (5), 662.

Sassa, S., Sekiguchi, H., 1999. Wave-induced liquefaction of beds of sand in a centrifuge. Geotechnique 49 (5), 621–638.

Sassa, S., Sekiguchi, H., Miyamoto, J., 2001. Analysis of progressive liquefaction as a moving-boundary problem. Ǵeotechnique 51 (10), 847–857.

Seed, H.B., Rahman, M.S., 1978. Wave-induced pore pressure in relation to ocean floor stability of cohesionless soils. Mar. Georesour. Geotechnol. 3 (2), 123–150.

Sumer, B.M., Fredsøe, J., Christensen, S., Lind, M.T., 1999. Sinking/floatation of pipelines and other objects in liquefied soil under waves. Coast. Eng. 38 (2), 53–90.

Sumer, B.M., Hatipoglu, F., Fredsøe, J., et al., 2006. The sequence of sediment behaviour during wave-induced liquefaction. Sedimentology 53 (3), 611–629.

Sumer, B.M., Kirca, V.S.O., Fredsøe, J., 2012. Experimental validation of a mathematical model for seabed liquefaction under waves. Int. J. Offshore Polar Eng. 22 (02).

Sumer, B.M., 2014. Liquefaction Around Marine Structures. World Scientific Publishing Co., Singapore.

Teh, T.C., Palmer, A., Damgaard, J., 2003. Experimental study of marine pipelines on unstable and liquefied seabed. Coast. Eng. 50 (1-2), 1–17.

Ülker, M.B.C., 2021. A combined theoretical and numerical modeling study of cyclic nonlinear response of sandy seabed. Ocean Eng. 219, 108348.

Yamamoto, T., Koning, H.L., Sellmeijer, H., Hijum, E.V., 1978. On the response of a poro-elastic bed to water waves. J. Fluid Mech. 87 (1), 193–206.

Zen, K., Yamazaki, H., 1990. Mechanism of wave-induced liquefaction and densification in seabed. Soils Found. 30 (4), 90–104.